OUTFLOW AND DENSE GAS EMISSION FROM MASSIVE INFRARED DARK CLOUDS

H. Beuther[1] and T. K. Sridharan[2]

ABSTRACT

Infrared dark clouds are expected to harbor sources in different, very young evolutionary stages. To better characterize these differences, we observed a sample of 43 massive infrared dark clouds, originally selected as candidate high-mass starless cores, with the IRAM 30 m telescope covering spectral line tracers of low-density gas, high-density gas, molecular outflows/jets and temperature effects. The SiO(2–1) observations reveal detections toward 18 sources. Assuming that SiO is exclusively produced by sputtering from dust grains, this implies that at least in 40% of this sample star formation is ongoing. A broad range of SiO line widths is observed (between 2.2 and 65 km s^{-1}), and we discuss potential origins for this velocity spread. While the low-density tracers ^{12}CO(2–1) and ^{13}CO(1–0) are detected in several velocity components, the high-density tracer H^{13}CO$^+$(1–0) generally shows only a single velocity component and is hence well suited for kinematic distance estimates of IRDCs. Furthermore, the H^{13}CO$^+$ line width is on average 1.5 times larger than that of previously observed NH$_3$(1, 1). This is indicative of more motion at the denser core centers, due to either turbulence or beginning star formation activity. In addition, we detect CH$_3$CN toward only six sources, whereas CH$_3$OH is observed toward approximately 40% of the sample. Estimates of the CH$_3$CN and CH$_3$OH abundances are low with average values of 1.2×10^{-10} and 4.3×10^{-10}, respectively. These results are consistent with chemical models at the earliest evolutionary stages of high-mass star formation. Furthermore, the CH$_3$OH abundances compare well to recently reported values for low-mass starless cores.

Subject headings: ISM: abundances — ISM: clouds — ISM: jets and outflows —
ISM: kinematics and dynamics — stars: early-type — stars: formation

1. INTRODUCTION

While observational research in high-mas star formation over the last few decades has focused on relatively evolved regions such as ultracompact H II regions (UCHIIs) and high-mass protostellar objects (HMPOs) (e.g., see reviews by Kurtz et al. 2000; Churchwell 2002; Beuther et al. 2007), the earliest stages of massive star formation have become regularly accessible only with the advent of large-scale mid-infrared surveys of the Galactic plane by satellite missions such as the *Infrared Space Observatory* (*ISO*), the *Midcourse Space Experiment* (*MSX*), and most recently *Spitzer*. The basic observational characteristics of the earliest stages of (massive) star formation, prior to the formation of any embedded heating source, should be that they are strong cold dust emitters at (sub)millimeter wavelengths, and have weak or nondetections in the mid-infrared because they have not yet heated a warm dust cocoon. In the low-mass regime, so-called infrared-dark clouds (IRDCs) have been studied regularly for a decade (e.g., Egan et al. 1998; Carey et al. 2000; Bacmann et al. 2000); in high-mass star formation the focus has shifted to these objects only more recently (e.g., Sridharan et al. 2005; Hill et al. 2005; Klein et al. 2005; Simon et al. 2006; Beltrán et al. 2006; Rathborne et al. 2006; Pillai et al. 2006).

Massive IRDCs (hereafter referred to simply as IRDCs) are not a well-defined class, but they likely harbor various evolutionary stages, from genuine high-mass starless cores (HMSCs) to high-mass cores harboring accreting low/intermediate-mass protostars, to the youngest HMPOs (Beuther et al. 2007). While the first stage provides good targets to study the initial conditions

of massive star formation prior to cloud collapse, the other stages are important to understanding the early evolution of massive star-forming clumps. Here we target a sample of massive IRDCs first identified as candidate HMSCs by Sridharan et al. (2005) in order to differentiate between the different evolutionary stages existing within this sample. To facilitate this, we observed the target sample with the IRAM 30 m telescope in different spectral lines sensitive to various physical processes such as molecular outflows (e.g., SiO, CO), dense gas (e.g., H^{13}CO$^+$, CH$_3$CN, CH$_3$OH), or hot core conditions (CH$_3$CN, CH$_3$OH). Table 1 lists the observed spectral lines, the upper level excitation energies $E_{\rm upper}$, and the critical densities $n_{\rm crit}$.

2. OBSERVATIONS AND DATA REDUCTION

We observed a sample of 43 IRDCs selected from Sridharan et al. (2005) in 2005 August at the IRAM 30 m telescope on Pico Veleta with four receivers simultaneously. The flexible multireceiver setup of the 30 m telescope allowed us to observe usually a few lines within the same spectral setup of each receiver: (1) H^{13}CO$^+$(1–0) and SiO(2–1), (2) ^{13}CO(1–0) and CH$_3$CN, (3) ^{12}CO(2–1), and (4) CH$_3$OH. Table 1 lists the corresponding frequencies, the spectral resolution, and the system temperatures for each line. The observations were conducted in a position-switching mode with OFF positions carefully chosen from the Massachusetts–Stony Brook Galactic plane CO survey (Sanders et al. 1986), usually approximately to the order 1000″ offset from the source positions.

3. RESULTS AND DISCUSSION

3.1. ^{12}CO(2–1), ^{13}CO(1–0) and H^{13}CO$^+$(1–0)

Figure 1 shows the ^{12}CO(2–1), ^{13}CO(1–0), and H^{13}CO$^+$(1–0) spectra for the whole source sample. Except for IRDC 18431−0312-4, where the H^{13}CO$^+$(1–0) line remained undetected,

[1] Max-Planck-Institute for Astronomy, Königstuhl 17, 69117 Heidelberg, Germany; beuther@mpia.de.
[2] Harvard-Smithsonian Center for Astrophysics, 60 Garden Street, Cambridge, MA 02138; tksridha@cfa.harvard.edu.

TABLE 1
Observing Parameters

Line	Frequency (GHz)	Δv (km s^{-1})	T_{sys}[a] (K)	1 σ rms[a] (K)	E_{upper} (K)	n_{crit}[b] (cm^{-3})
H^{13}CO$^+$(1–0)...............	86.754	1.1	110	0.02	4.2	1.7E5
SiO(2–1)......................	86.847	1.1	110	0.02	6.3	7.3E5
^{13}CO(1–0)....................	110.201	0.9	220	0.04	5.3	2.2E3
CH$_3$CN(6$_0$–5$_0$)............	110.384	0.9	220	0.03	18.5	1.5E6[c]
CH$_3$CN(6$_1$–5$_1$)..............	110.381	0.9	220	0.03	25.7	1.5E6[c]
CH$_3$CN(6$_2$–5$_2$).............	110.375	0.9	220	0.03	47.1	1.6E6[c]
^{12}CO(2–1)	230.538	1.6	660	0.30	16.6	1.0E4
CH$_3$OH(5$_1$–4$_1$)E.........	241.879	1.2	760	0.13	55.9	1.1E6
CH$_3$OH(5$_0$–4$_0$)$A+$	241.791	1.2	760	0.13	34.8	[d]
CH$_3$OH(5$_{-1}$–4$_{-1}$)E	241.767	1.2	760	0.13	40.4	9.5E5
CH$_3$OH(5$_0$–4$_0$)E	241.700	1.2	760	0.13	47.9	1.0E6

[a] Average system temperature and 1 σ rms values.
[b] Calculated from $A = 0.3\lambda_{100}^{-3}\mu^2$ (λ_{100} in units of 100 μm and $\mu = 3.9$ debye) and γ(CH$_3$CN(6–5))$_{20 K}$ from Pei & Zeng (1995a, 1995b).
[c] $n_{crit} = A/\gamma$ with the Einstein coefficient A and the collisional rate γ. Except for CH$_3$CN, A and γ were taken from LAMBDA (Schöier et al. 2005) at $T = 20$ K.
[d] No data for this transition in LAMBDA.

toward all other sources the three lines were detected. The most obvious difference between ^{12}CO/^{13}CO on the one hand and H^{13}CO$^+$ on the other is that the CO isotopologues are detected at many different velocities, while H^{13}CO$^+$ usually only shows a single spectral peak (except for a few double-peaked structures listed in Table 2). This difference can be explained straightforwardly by the location of the sources within the Galactic plane, since CO traces more or less all molecular clouds along the line of sight, and so contributions from various Galactic spiral arms, whereas H^{13}CO$^+$ has significantly higher critical densities (Table 1) and thus traces only the dense cores we are interested in. Therefore, if one wants to know the velocity of a specific region, CO observations are not as useful as high-density tracers. The peak velocities v of H^{13}CO$^+$ (Table 2) correspond well to the previously derived velocities from NH$_3$ observations of the same sample (Sridharan et al. 2005). Identifying the correct associated velocity component to derive accurate velocities is an important step to obtaining distance estimates from the Galactic rotation curve as reported in Brand & Blitz (1993) and Sridharan et al. (2005).

Table 2 also lists the full width half-maximum (FWHM) line widths Δv(H^{13}CO$^+$) of the observed H^{13}CO$^+$ lines from Gaussian fits; the average H^{13}CO$^+$ line width is 2.6 km s^{-1}. Figure 2 shows a comparison of the H^{13}CO$^+$ line width with the previously derived line width from the NH$_3$(1, 1) observations from (Sridharan et al. 2005). We find that the H^{13}CO$^+$ line width nearly always exceeds the line width from the NH$_3$(1, 1) with an average line width ratio

$$\frac{\Delta v(\mathrm{H}^{13}\mathrm{CO}^+(1-0))}{\Delta v(\mathrm{NH}_3(1,1))} = 1.5.$$

This is interesting, since the critical densities for both molecules differ by about 2 orders of magnitude; n_{crit}(NH$_3$(1, 1)) $\sim 2 \times 10^3$ cm^{-3} (e.g., Zhou et al. 1989), n_{crit}(H^{13}CO$^+$(1 – 0)) $\sim 1.7 \times 10^5$ cm^{-3} (Table 1), whereas the thermal line widths ($\Delta v_{th} = [8\ln 2(kT/m_{mol})]^{1/2}$, with molecular mass m_{mol}) are similar [Δv_{th}(NH$_3$(1, 1))$_{15K} \sim 0.2$ km s^{-1} and Δv_{th}(H^{13}CO$^+$(1–0))$_{15K} \sim 0.15$ km s^{-1}), Δv_{th}(H^{13}CO$^+$(1 – 0)) being even smaller

than Δv_{th}(NH$_3$(1, 1)) because of its larger molecular weight. Therefore, differences in the nonthermal motions have to be responsible for the line width variations between both species. Similar results were obtained for low-mass cores in a comparison of CS with NH$_3$ line widths (Zhou et al. 1989).

There are several potential explanations for such a line width difference. For example, there is the well-known line width–size relation $\Delta v \propto R^{0.5}$ (Larson 1981). This relation would imply that our target regions would be on average 2.3 times larger in H^{13}CO$^+$ than they are in NH$_3$. Although we have no maps of the regions, this appears very unlikely. A different possibility was discussed by Zhou et al. (1989) and Myers & Benson (1983): if the stability of a core is determined by the entire line broadening, for a gravitationally stable core the critical density should relate to the line width and size of a molecular core as

$$n_{crit} \propto (\Delta v/R)^2 \iff \Delta v \propto R\sqrt{n_{crit}}.$$

To fulfill this criterion, the H^{13}CO$^+$ source size would need to be $\sim$7 times smaller than that of NH$_3$, which again appears to be very unlikely. In this scenario, one could then conclude that molecular clumps are not gravitationally stable but may already be collapsing. However, overall collapse is not certain from such an analysis, and the clumps could also be fragmenting or only partially collapsing (see discussion in Zhou et al. 1989).

As discussed below in § 3.2, a significant fraction of sources exhibits broad line wings in the jet/outflow tracer SiO, which is indicative of early outflow and hence early star formation activity. Since H^{13}CO$^+$ has a larger critical density, it traces denser regions of the gas clumps. With ongoing star formation activity, one expects additional line broadening effects from various physical processes such as outflows, infall, and potential rotation of embedded accretion disks, all spatially unresolved by the current observations. Most of these effects are likely contributing more strongly in the dense gas components and hence could explain the excess in H^{13}CO$^+$ line width.

3.2. SiO(2–1)

One of the aims of this study was to identify how many of the sources would show clear SiO emission caused by molecular outflow activity. SiO is believed to be produced in the gas phase after sputtering Si-bearing species from the dust grain surfaces when the outflow/jet impinges on the ambient gas and dust (Schilke et al. 1997). SiO is usually barely detectable in quiescent clouds. Figure 3 presents the 18 SiO(2–1) detections toward our source sample of 43 regions. If this source sample is representative for typical infrared-dark clouds, this implies that in at least 40% of the IRDCs, star formation has already started (the absence of SiO emission does not necessarily imply absence of star formation activity). However, it is not obvious whether this sample is representative of all IRDCs, because it was selected to be close to sites of already ongoing massive star formation.

Table 2 also lists the width-to-zero-velocity Δv_0 of the observed SiO(2–1) lines. If one divides the observed SiO spectra by their width-to-zero-velocity Δv_0 into three regimes, (1) low velocity, $\Delta v_0 < 10$ km s^{-1}; (2) intermediate velocity, 10 km s^{-1} < $\Delta v_0 < 20$ km s^{-1}; and (3) high velocity, $\Delta v_0 > 20$ km s^{-1}, one finds six sources in the low-velocity regime, five at intermediate velocities, and seven in the high-velocity regime. While the

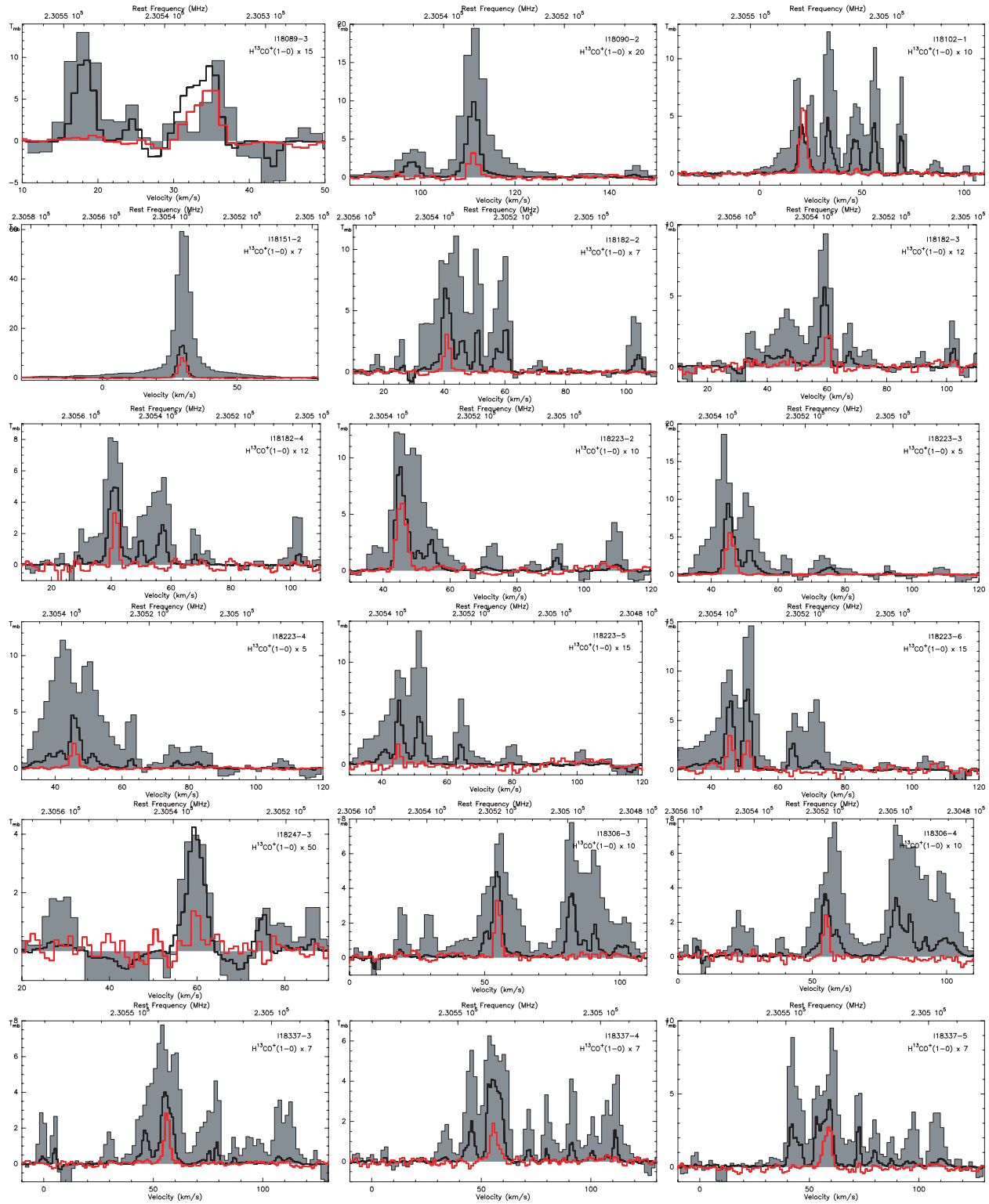Fig. 1.—^{12}CO(2–1) (*gray line*), ^{13}CO(1–0) (*black line*), and H^{13}CO^{+}(1–0) (*red line*) spectra toward the whole sample of IRDCs. The H^{13}CO^{+}(1–0) spectra are scaled up by the factor labeled in each panel for presentation purposes.
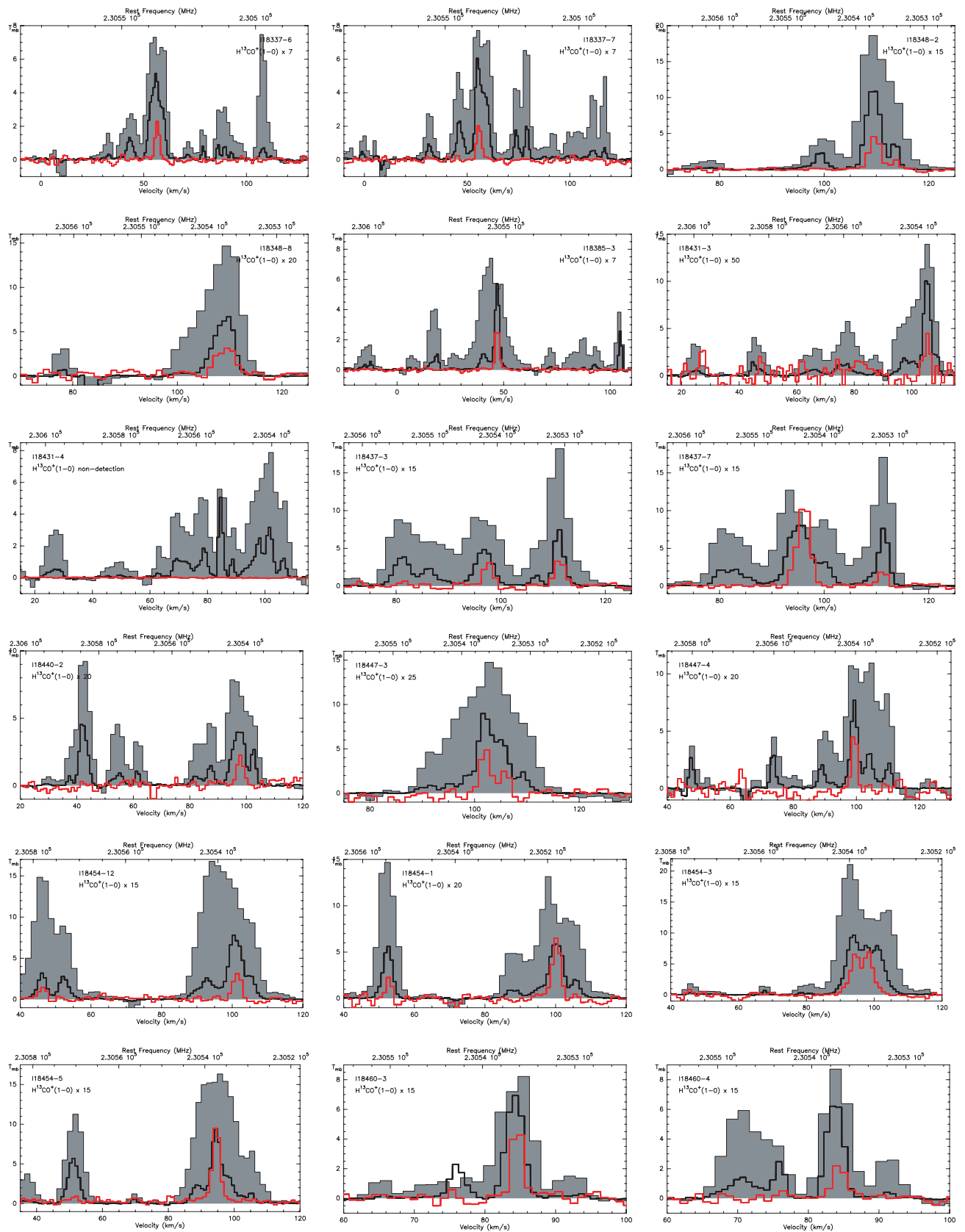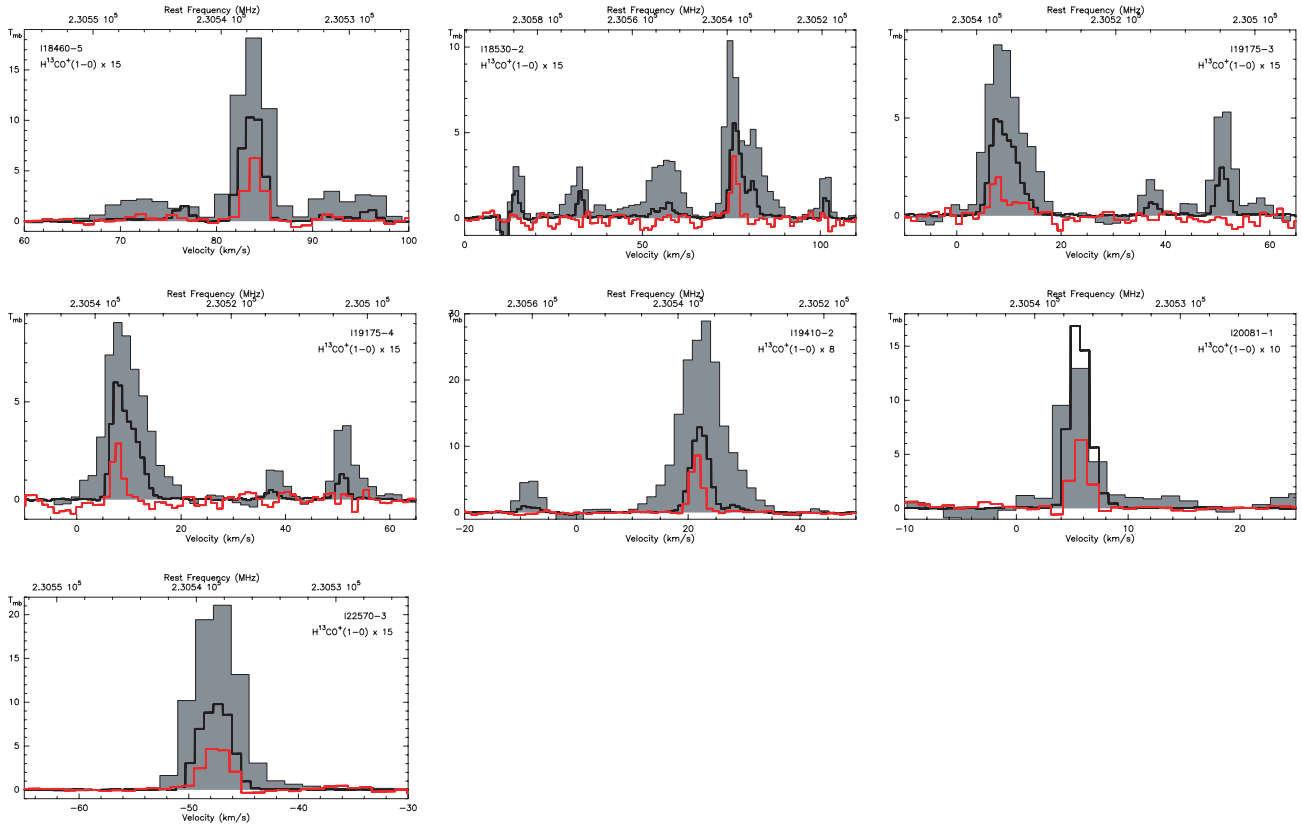
FIG. 1—*Continued*

351

Fig. 1—*Continued*

sources at intermediate to high velocities obviously show gas at relatively high velocities with respect to the ambient gas, this is less clear for the sources in the low-velocity regime: those sources with $\Delta v_0 > 5$ km s^{-1} probably also have outflow contributions, but the SiO(2–1) spectra toward two sources with $\Delta v_0 < 2.5$ km s^{-1} (IRDC 18223-6 and IRDC 18530-2) hardly look like typical outflow spectra. A similar spread in SiO velocities has also previously been observed by, e.g., Lefloch et al. (1998) and Codella et al. (1999). What are some possible reasons for the different observed SiO Δv_0?

The observed velocity spread could partly be produced by the angles between the outflows and the plane of the sky, since we only observe line-of-sight velocities. However, assuming a random distribution of outflow inclination angles θ ($\theta = 0$ is an outflow along the line of sight) and similar unprojected outflow velocities, one would expect fewer outflows at high velocities than at low velocities [$\int_0^{45} \sin(\theta)d\theta \sim 0.29$ vs. $\int_{45}^{90} \sin(\theta)d\theta \sim 0.71$]. This is in contrast to our relatively even distribution of Δv_0 from low to high values. Hence, inclination effects are unlikely to explain the observations.

Outflows/jets from massive protostars have intrinsically higher velocities than their low-mass counterparts (e.g., Richer et al. 2000). In addition, more luminous sources usually exhibit stronger SiO emission (e.g., Codella et al. 1999). Therefore, the sources with smaller line widths could harbor less massive protostars that may or may not form a massive star at the end of their evolution. Furthermore, all objects with low SiO velocity spreads are also the weakest or nondetections in CH$_3$CN and CH$_3$OH (see § 3.3), which is also expected in the framework of embedded protostars with different masses. Thus, different masses/luminosities of the embedded outflow-driving sources could potentially cause the observed SiO line width difference.

Since IRDCs are believed to represent the earliest evolutionary stages of massive (and low-mass) star formation, we expect that low- to intermediate-mass protostars may be embedded in some of them, which are likely destined to grow, accrete, and become high-mass stars at the end of their evolution (e.g., IRDC 18223-3; Beuther et al. 2005a; Beuther & Steinacker 2007). However, a priori we cannot tell whether an object will become massive at the end of its evolution or whether it will remain a low-mass protostar. In this scenario, one can also speculate about an evolutionary sequence in which the growing protostars accelerates the gas to higher velocities in the course of its early evolution, i.e., the smaller line widths may correspond to the still less massive and younger objects, whereas the broad line width sources may have already accreted more mass and could hence be a little bit more evolved. This picture is consistent with the assertion that the line width distribution may depend on the mass and luminosity of the central object, with the additional assumption that the lower mass objects may still be able to become massive stars during their ongoing evolution. This scenario may appear counterintuitive compared to typical low-mass outflows, in which the strongest emission is observed from class 0 sources and the SiO emission gets weaker for more evolved class I and II sources (e.g., Gibb et al. 2004). However, even class 0 sources already typically have ages of the order of 10^4 yr, and IRDCs similar to those presented here are likely still significantly younger (e.g., Beuther & Steinacker 2007; Krumholz et al. 2007). Furthermore, this low-mass classification scheme is unlikely to be applicable to high-mass star formation, since, among other reasons, massive stars reach the main sequence while accretion processes can still be ongoing (e.g., Schaller et al. 1992; McKee & Tan 2003). Therefore, our picture applies only to the earliest evolutionary stages of strongly

TABLE 2
SOURCE PARAMETERS

Name	R.A. (J2000)	Decl. (J2000)	D^a (kpc)	$v(H^{13}CO^+)$ (km s^{-1})	$\Delta v(H^{13}CO^+)$ (km s^{-1})	$\Delta v_0(SiO)^b$ (km s^{-1})	$S_{1.2\ mm}{}^c$ (mJy/(11″)^2)	$N_{H_2}{}^d$ (×10^{23} cm^{-2})
IRDC 18089−1732-3	18 11 45.3	−17 30 38	3.6	34.2 ± 0.1	3.9 ± 0.2	5.5	147	1.5
IRDC 18090−1832-2	18 12 02.0	−18 31 27	6.6	111.2 ± 0.1	2.2 ± 0.2		89	0.9
IRDC 18102−1800-1	18 13 11.0	−18 00 23	2.7^e	21.4 ± 0.1	3.4 ± 0.1	42.2	632	6.3
IRDC 18151−1208-2	18 17 50.3	−12 07 54	3.0	29.8 ± 0.1	3.0 ± 0.1	65.0^h	620	6.2
IRDC 18182−1433-2	18 21 14.9	−14 33 06	3.6	40.9 ± 0.1	2.2 ± 0.1		144	1.4
IRDC 18182−1433-3	18 21 17.5	−14 29 43	4.6^e	60.2 ± 0.1	1.7 ± 0.3	5.5		
IRDC 18182−1433-4	18 21 14.0	−14 34 20	3.6	41.4 ± 0.1	2.0 ± 0.2			
IRDC 18223−1243-2	18 25 10.0	−12 44 00	3.7	45.5 ± 0.1	3.4 ± 0.1		156	1.6
IRDC 18223−1243-3	18 25 08.3	−12 45 27	3.7	45.7 ± 0.1	2.7 ± 0.1	35.5	289	2.9
IRDC 18223−1243-4	18 25 06.8	−12 48 00	3.7	45.7 ± 0.1	2.4 ± 0.1	38.9	77	0.8
IRDC 18223−1243-5	18 25 12.0	−12 53 23	3.7	45.1 ± 0.2	1.7 ± 0.2			
IRDC 18223−1243-6^f	18 25 16.2	−12 55 33	3.7	45.7 ± 0.1	2.0 ± 0.3	2.4		
IRDC 18223−1243-6^f	18 25 16.2	−12 55 33	3.7	50.9 ± 0.2	2.1 ± 0.4			
IRDC 18247−1147-3	18 27 31.0	−11 44 46	6.7	59.7 ± 0.2	2.2 ± 0.6		110	1.1
IRDC 18306−0835-3	18 33 32.1	−08 32 28	3.8^e	54.8 ± 0.1	2.4 ± 0.1		154	1.5
IRDC 18306−0835-4	18 33 34.8	−08 31 20	3.8^e	55.2 ± 0.1	2.4 ± 0.2			
IRDC 18337−0743-3	18 36 18.2	−07 41 00	4.0	56.2 ± 0.1	2.8 ± 0.1	39.8	123	1.2
IRDC 18337−0743-4	18 36 29.9	−07 42 05	4.0	55.8 ± 0.1	4.2 ± 0.3			
IRDC 18337−0743-5	18 36 41.0	−07 39 56	4.0	58.4 ± 0.1	4.1 ± 0.2	16.2		
IRDC 18337−0743-6	18 36 36.0	−07 42 17	4.0	56.6 ± 0.1	2.5 ± 0.2			
IRDC 18337−0743-7	18 36 19.0	−07 41 48	4.0	55.9 ± 0.1	2.7 ± 0.2			
IRDC 18348−0616-2	18 37 27.6	−06 14 08	6.3	109.7 ± 0.1	2.6 ± 0.1	9.9	169	1.7
IRDC 18348−0616-8	18 37 14.7	−06 17 25	6.3	109.3 ± 0.2	4.4 ± 0.4			
IRDC 18385−0512-3	18 41 17.4	−05 10 03	3.3^e	47.0 ± 0.1	2.1 ± 0.1	41.1	77	0.8
IRDC 18431−0312-3	18 45 45.0	−03 08 56	6.6^e	105.4 ± 0.3	2.2 ± 0.7			
IRDC 18431−0312-4	18 45 53.0	−03 09 01		nondet.	nondet.			
IRDC 18437−0216-3^f	18 46 21.9	−02 12 24	6.2^e	97.6 ± 0.2	2.1 ± 0.4		96	1.0
IRDC 18437−0216-3^f	18 46 21.9	−02 12 24	7.3^e	111.3 ± 0.1	2.3 ± 0.4		96	1.0
IRDC 18437−0216-7^f	18 46 22.0	−02 14 10	6.2^e	96.1 ± 0.1	2.9 ± 0.1	13.0		
IRDC 18437−0216-7^f	18 46 22.0	−02 14 10	7.3^e	111.2 ± 0.7	1.9 ± 1.8			
IRDC 18440−0148-2	18 46 31.0	−01 47 08	5.6^e	97.9 ± 0.2	2.9 ± 0.4			
IRDC 18447−0229-3	18 47 42.0	−02 25 12	6.4^e	102.1 ± 0.2	2.6 ± 0.5			
IRDC 18447−0229-4	18 47 38.9	−02 28 00	6.4^e	99.4 ± 0.1	1.9 ± 0.3			
IRDC 18454−0158-1^f	18 48 02.1	−01 53 56	3.5^e	52.8 ± 0.4	1.7 ± 0.7		178	1.8
IRDC 18454−0158-1^f	18 48 02.1	−01 53 56	6.4^e	100.2 ± 0.1	2.7 ± 0.2	10.9	178	1.8
IRDC 18454−0158-3^f	18 47 55.8	−01 53 34	6.0^e	94.3 ± 0.1	3.5 ± 0.3	17.3^g	204	2.0
IRDC 18454−0158-3^f	18 47 55.8	−01 53 34	6.4^e	98.4 ± 0.1	3.3 ± 0.3	17.3^g	204	2.0
IRDC 18454−0158-5	18 47 58.1	−01 56 10	6.0^e	94.6 ± 0.1	2.7 ± 0.1	17.8	102	1.0
IRDC 18454−0158-12^f	18 48 05.7	−01 53 28	3.1^e	46.3 ± 0.4	2.5 ± 0.8			
IRDC 18454−0158-12^f	18 48 05.7	−01 53 28	6.4^e	101.4 ± 0.1	2.7 ± 0.3			
IRDC 18460−0307-3	18 48 36.0	−03 03 49	5.2	84.6 ± 0.1	1.8 ± 0.2		84	0.8
IRDC 18460−0307-4	18 48 46.0	−03 04 05	5.2	84.4 ± 0.1	2.4 ± 0.3		177	1.8
IRDC 18460−0307-5	18 48 47.0	−03 01 29	5.2	84.0 ± 0.1	2.1 ± 0.1		74	0.7
IRDC 18530+0215-2	18 55 29.0	+02 17 43	5.0^e	75.9 ± 0.1	2.1 ± 0.2	2.2		
IRDC 19175+1357-3	19 19 52.1	+14 01 52	1.1	7.7 ± 0.2	2.9 ± 0.7		53	0.5
IRDC 19175+1357-4	19 19 50.6	+14 01 22	1.1	7.8 ± 0.1	2.1 ± 0.2		87	0.9
IRDC 19410+2336-2	19 43 10.2	+23 45 04	2.1	21.5 ± 0.1	2.3 ± 0.1	36.8^h	343	3.4
IRDC 20081+2720-1	20 10 13.0	+27 28 18	0.7	5.7 ± 0.1	1.8 ± 0.1		244	2.4
IRDC 22570+5912-3	22 58 55.1	+59 28 33	5.1	-47.5 ± 0.1	2.8 ± 0.1	5.5	88	0.9

[a] Most distances are taken from Sridharan et al. (2005). The exceptions are marked.

[b] Width of SiO(2–1) line down to zero intensity.

[c] Here we present the 1.2 mm peak fluxes extracted directly from the peak positions. In the original paper, Beuther et al. (2002) present peak fluxes from 2D Gaussian fits, which are on average a bit lower.

[d] The column density calculations follow Beuther et al. (2005b) at an average temperature of 19 K to be better comparable with the CH_3OH and CH_3CN column densities calculated at $T = 18.75$. Masses and integrated fluxes were already presented in Sridharan et al. (2005).

[e] Newly derived near kinematic distances following Brand & Blitz (1993), because IRDCs at the far distances are unlikely.

[f] Rows with the same IRDC name correspond to different $H^{13}CO^+$ velocity components.

[g] This is a line blend between both velocity components.

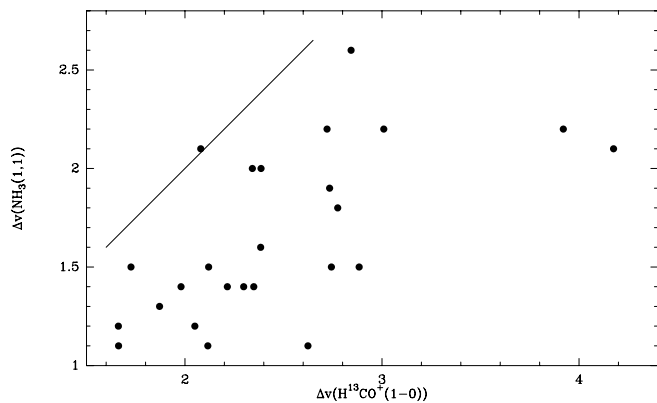[h] The outflow was studied in detail by Beuther et al. (2003).

F$_{IG.}$ 2.—Comparison of line widths between H^{13}CO$^+$(1–0) (this work) and NH$_3$(1, 1) (Sridharan et al. 2005).

accreting protostars destined to become massive stars at the end of their evolution. In principle, the nondetection of SiO line wings could also be caused by poorer signal-to-noise ratios or larger distances to the respective region. However, neither scenario is likely to be the case here, because we have approximately the same rms for all sources, and the line width differences are found also toward sources at the same distances (e.g., IRDC 18223−1243-3 and IRDC 18223−1243-4 vs. IRDC 18223−1243-6).

Do the $\Delta v_0 < 2.5$ km s^{-1} fit into any of these pictures? Since more than 50% of the target sources exhibit no SiO emission at all down to our sensitivity limit, it is interesting that two objects show these extremely narrow line widths. Lefloch et al. (1998) and Codella et al. (1999) try to explain similar observations by outflow/dense clump interactions and with an outflow evolutionary model. In the latter scenario, the highest velocity components are found at the earliest evolutionary class 0 stages, and the smaller line width components could be remnants from earlier interactions of molecular outflows with the ambient gas (Codella et al. 1999). They estimated the corresponding time-scale to decrease the SiO emission and the velocities to be of the order of 10^4 yr. We consider this scenario unlikely for our sample, because massive star formation proceeds on relatively short timescales (of the order of 10^5 yr; McKee & Tan 2002), and after 10^4 yr the regions are expected to be strong enough to be detectable at near- and mid-infrared wavelengths (e.g., the samples presented by Molinari et al. 1996 or Sridharan et al. 2002), which is in contrast to our sample selection as infrared dark clouds. Another possibility is to speculate whether these objects could represent the earliest observed stage of star formation within our source sample: in this picture, the Si-bearing species would just be released from the grains by shock interaction, and SiO would only have begun to form in the gas phase, but the young jet/outflow would not yet have had the time to accelerate large amounts of gas to detectable higher velocities. To confirm or reject this picture, additional indicators of star formation activity need to be observed, e.g., infall of gas via asymmetric line profiles (e.g., Myers et al. 1996) or shocked H$_2$ emission in either the K band (e.g., Davis et al. 2004) or the IRAC 4.5 μm band (e.g., Rathborne et al. 2005).

3.3. CH$_3$CN(6$_k$–5$_k$) and CH$_3$OH(5–4)

In addition to the previously discussed molecules, the spectral setup also allowed us to observe the typical hot-core tracer CH$_3$CN, as well as a series of four CH$_3$OH lines. Although the critical densities and excitation parameters of the two molecules do not differ that much (see Table 1), CH$_3$OH typically has 1–2 orders of magnitude larger gas column densities and is hence easier to observe (e.g., van Dishoeck & Blake 1998; Nomura & Millar 2004). Furthermore, CH$_3$OH is known to be present in massive star formation right from the beginning, and hence it is a so-called parent molecule, whereas CH$_3$CN is a daughter molecule, which needs time to form through chemical processes during the massive star formation process (e.g., Nomura & Millar 2004). Therefore, toward a sample of young IRDCs, one would expect CH$_3$CN to be either undetectable or only weakly detected in a few sources, whereas CH$_3$OH should be detectable toward a larger fraction of the sample.

These expectations are largely confirmed by our observations (Figs. 4 and 5); we detect CH$_3$CN only toward 6 sources (∼14%), whereas CH$_3$OH is observed toward 17 regions (∼40%). Furthermore, if detected, CH$_3$CN(6$_k$–5$_k$) is observed only in its two lowest k-components with excitation temperatures <30 K, the $k = 2$ transition is detected in no source at all. Similarly, for CH$_3$OH, we detected toward the 17 regions the two lower excitation lines, whereas the two higher excitation lines are detected only toward a small subsample of 5 regions. This is additional confirmation of the youth and low average temperatures of the selected source sample. Table 3 lists the line widths $\Delta\nu_{k=0}$ and $\Delta\nu_{k=1}$ of the CH$_3$CN $k = 0, 1$ components from Gaussian fits to each line. While we cannot fit one source because of multiple components, and in one other source $\Delta\nu_{k=0}$ and $\Delta\nu_{k=1}$ are of approximately equal width; for the four other sources we find consistently larger line widths in the $k = 1$ component than in the $k = 0$ component. This is consistent with already ongoing star formation activity in these regions, where the warmer, more central gas is subject to more nonthermal motion, either of a turbulent nature or due to infall, rotation, and/or outflow processes.

One can try to use the observed lines also to get more quantitative temperature and column density estimates. Following Loren & Mundy (1984), assuming optically thin emission and that a single temperature characterizes the populations within a k-ladder and between different k-ladders, the ratios of the intensities of different k lines can be used to estimate this temperature. Specifically, for the $J = 6–5$ line and $k = 0$ and $k = 1$ components, we have

$$T = 7.2/\ln(I_0/I_1),$$

with I_k the corresponding observed peak intensities. For IRDC 18102−1800-1 and IRDC 20081+2720-2, the relative line intensities are consistent with optically thin emission, and we estimate the temperatures to be 16 ± 16 and 16 ± 13 K, respectively. For the other sources, while they are unlikely to be optically thick, the intensities are inconsistent with optically thin emission, so we do not estimate temperatures. It is interesting that the estimates, where possible, although not very accurate, turn out to be low and similar to estimates from NH$_3$ observations (Sridharan et al. 2005). We cannot use the two mainly detected CH$_3$OH lines for temperature estimates, because they are of different symmetry (A- and E-CH$_3$OH) and can be considered for radiative transport purposes as distinct molecules.

However, we can calculate the column densities in the detected CH$_3$OH and CH$_3$CN lines, and then derive the total molecular column densities following Rohlfs & Wilson (2006). As partition functions, we used the values listed in the JPL catalog
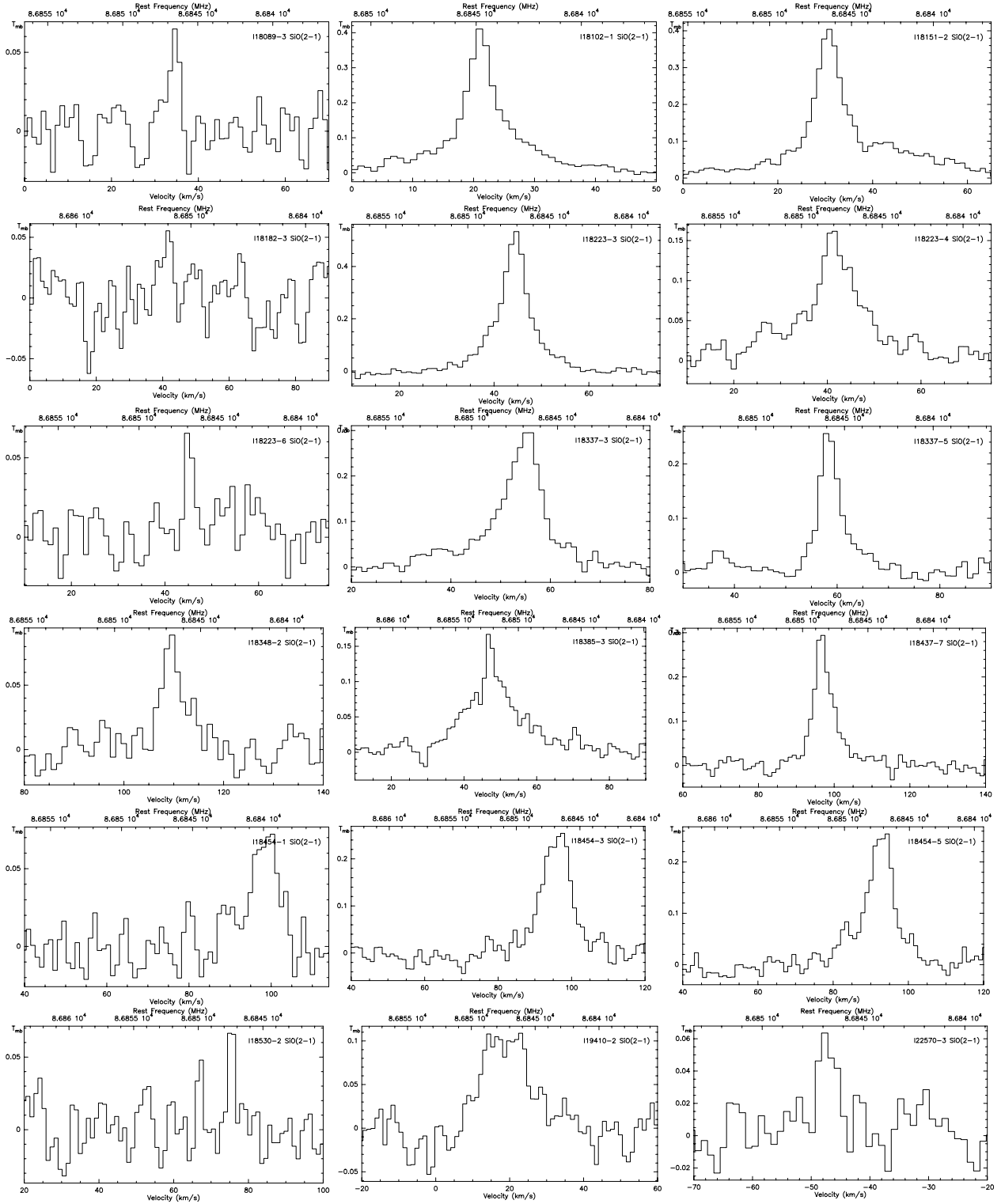
Fig. 3.—SiO(2–1) detections.

at $T = 18.75$ K (Poynter & Pickett 1985). Furthermore, we are interested in CH_3OH and CH_3CN molecular abundances. To estimate these, we extracted the 1.2 mm peak fluxes from the images presented in Beuther et al. (2002).[3] Following Hildebrand

(1983) and Beuther et al. (2005b), we then calculated the H_2 column densities at $T = 19$ K (corresponding to the partition functions for the molecular emission), assuming optically thin emission and a dust opacity index $\beta = 2$. The spatial resolution of the 1.2 mm and CH_3OH data is approximately the same; for comparison with the lower resolution CH_3CN data, we also smoothed the 1.2 mm images to the corresponding spatial resolution of 23″. The 1.2 mm peak fluxes and H_2 column densities

---

[3] Beuther et al. (2002) presented peak fluxes from 2D Gaussian fits to the images, whereas here we use the exact fluxes toward the peak positions. The former are on average a bit lower.
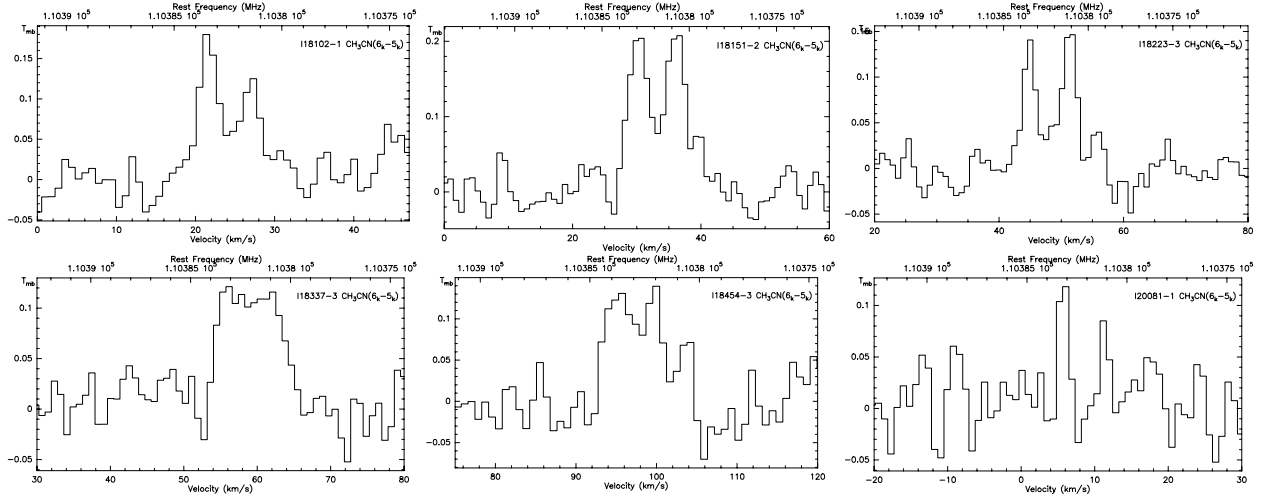
Fig. 4.—$CH_3CN(6_k-5_k)$ detections. The rest frequencies of the $k = 0, 1, 2$ components are at 110383.522, 110381.404, and 110375.052 MHz, respectively. Because of the small intrinsic line widths, the $k = 0, 1$ components are spectrally resolved, which is usually not the case for more evolved high-mass protostellar objects or hot molecular cores.

(both at $11''$ resolution) are listed in Table 2. The different H_2 column densities were then used to estimate the CH_3OH and CH_3CN abundances. The calculated molecular column densities are estimated to be correct to within a factor of 5; the accuracy of the estimated abundances is correspondingly worse. Table 3 lists the derived molecular CH_3OH and CH_3CN column densities and abundances, which are on average relatively low.

The average CH_3CN column density and abundance are 3.1×10^{12} cm^{-2} and 1.2×10^{-10}, respectively. This CH_3CN abundance compares well to the CH_3CN abundance observed, for example, in the relatively cold and quiescent Orion extended ridge, whereas it is 2 orders of magnitude below the values obtained for the Orion hot core (van Dishoeck & Blake 1998). Furthermore, it fits well with the chemical modeling of young high-mass star-forming regions by Nomura & Millar (2004); they find very low CH_3CN column densities of the order 10^{11}–10^{12} cm^{-2} after only a few hundred years, which then progressively increase to values $>10^{15}$ cm^{-2} after several 10^5 yr. In this picture, even the sources with detected CH_3CN emission are, as expected, extremely young massive star-forming regions.

The average CH_3OH column density and abundance are 8.2×10^{13} cm^{-2} and 4.3×10^{-10}, respectively. This abundance is orders of magnitude below the values obtained toward the typical regions in Orion (e.g., 8×10^{-9} for the extended ridge and 2×10^{-7} for the hot core; van Dishoeck & Blake 1998). However, it is very close to the recently reported CH_3OH abundances of 6×10^{-10} in the low-mass starless cores L1498 and L1517B (Tafalla et al. 2006). Although the statistics are still small, this similarity between CH_3OH abundances in low-mass starless cores and high-mass IRDCs indicates that the initial CH_3OH molecular abundances at early evolutionary stages do not differ significantly between low- and high-mass star-forming regions.

4. CONCLUSIONS AND SUMMARY

These single-dish millimeter spectral multiline observations toward a sample of 43 massive IRDCs revealed a range of interesting results. Since IRDC are expected to harbor sources in different evolutionary stages, from genuine HMSCs to high-mass cores with embedded low- to intermediate-mass protostars potentially destined to become massive stars, it is not surprising

that the observational signatures vary significantly over the sample. Because our spectral line selection covered tracers sensitive to different processes (outflows, dense gas, lower density gas, hot core chemistry) we are able to constrain various characteristics. In summary, these are:

1. Toward 40% of the sources, SiO(2–1) as a typical outflow/jet tracer was detected. Assuming that SiO is exclusively produced by gas phase reactions after sputtering Si-bearing species from dust grains, this implies that at least 40% of the IRDCs presented here have ongoing star formation activity (although nondetection of SiO does not imply no star formation activity; hence the lower limit). The observed width-to-zero-velocity of the SiO lines varies between 2.2 and 65 km s^{-1}. While inclination effects are unlikely to cause this velocity spread, we discuss other potential origins, e.g., embedded objects with different masses and/or possible evolutionary effects.

2. While we usually detect many velocity components in the low-density tracers $^{12}CO(2-1)$ and $^{13}CO(1-0)$, the high-density tracer $H^{13}CO^+(1-0)$ is also present in all except one source, but in general tracing only one velocity component. Therefore, it is well suited to derive velocities with respect to the standard of rest and hence kinematic distances for IRDCs. The observed FWHM line width of $H^{13}CO^+(1-0)$ is on average a factor 1.5 larger than that of the previously observed NH$_3$(1,1) line. Several possibilities for that behavior are discussed. While the typical line width–size relation is unlikely the cause for this behavior, the data are consistent with gravitational instabilities of the cores. However, this interpretation is not unambiguous. Since $H^{13}CO^+$ has higher critical densities, it traces the denser central cores with likely larger internal motions. This motions could be caused by turbulence or by active star formation processes such as outflows/infall and rotation.

3. As expected, CH_3CN is only rarely detected (toward $\sim$14% of the sources), whereas CH_3OH is observed toward a larger fraction of the sample ($\sim$40%). Both molecules are only detected in their lower energy transitions. While temperature estimates are hardly feasible with these data, we are able to derive the CH_3CN and CH_3OH abundances with average values of 1.2×10^{-10} and 4.3×10^{-10}, respectively. The low CH_3CN column densities are consistent with chemical models in which the CH_3CN abundances are very low at the earliest evolutionary stages and progressively increase with time. The derived CH_3OH abundances
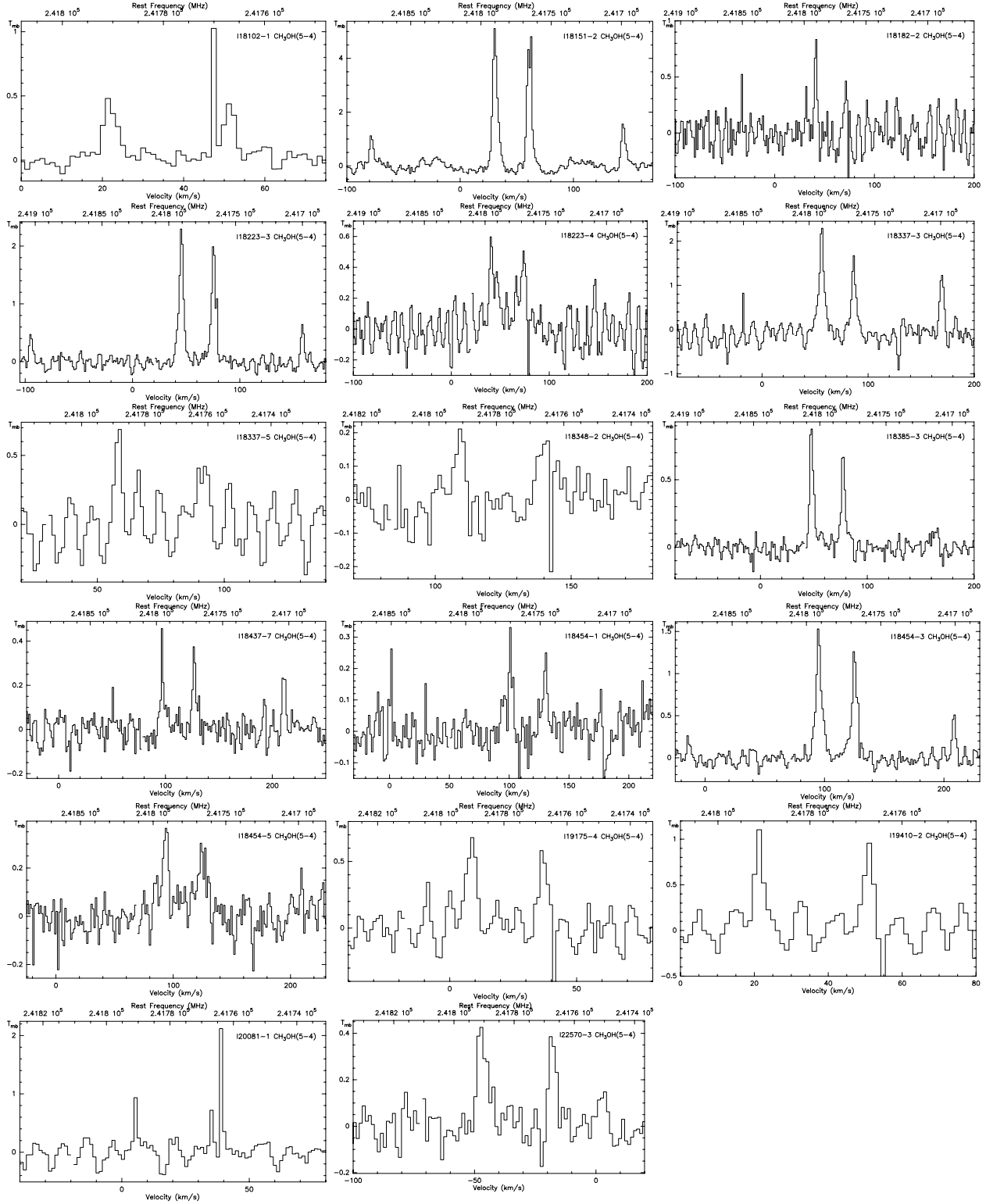
FIG. 5.—CH₃O(5−4) detections. The rest frequencies of the four detected lines are $CH_3OH(5_1-4_1)E$ at 241879.073 MHz, $CH_3OH(5_0-4_0)A+$ at 241791.431 MHz, $CH_3OH(5_{-1}-4_{-1})E$ at 241767.224 MHz, $CH_3OH(5_0-4_0)E$ at 241700.219 MHz. The few single-channel spikes are artifacts caused by the correlator.

BEUTHER & SRIDHARAN

TABLE 3
CH$_3$CN AND CH$_3$OH PARAMETERS

Name	$\Delta v_{k=0}$[a] (km s^{-1})	$\Delta v_{k=1}$[a] (km s^{-1})	N_{CH_3CN} ($\times 10^{12}$ cm^{-2})	X_{CH_3CN} ($\times 10^{-10}$)	N_{CH_3OH} ($\times 10^{13}$ cm^{-2})	X_{CH_3OH} ($\times 10^{-10}$)
IRDC 18102−1800-1	2.9 ± 0.4	3.9 ± 0.8	2.6	0.3	2.8	0.4
IRDC 18151−1208-2	3.4 ± 0.3	4.5 ± 0.5	5.3	0.8	37.2	6.0
IRDC 18182−1433-2					3.0	2.1
IRDC 18223−1243-3	2.8 ± 0.5	3.1 ± 0.5	2.7	0.9	17.6	6.1
IRDC 18223−1243-4					4.6	6.0
IRDC 18337−0743-3	3.1 ± 0.9	6.2 ± 1.4	4.4	3.6	13.1	10.7
IRDC 18385−0512-3					5.3	6.9
IRDC 18437−0216-7					2.5	−
IRDC 18454−0158-1					1.7	0.9
IRDC 18454−0158-1					1.7	0.9
IRDC 18454−0158-3	?[b]	?[b]			11.1	5.5
IRDC 18454−0158-3	?[b]	?[b]			11.1	5.5
IRDC 19175+1357-4					4.3	5.0
IRDC 19410+2336-2					5.0	1.5
IRDC 20081+2720-1	1.4 ± 0.3	1.3 ± 0.4	0.7	0.3		
IRDC 22570+5912-3					2.4	2.8

[a] Line width of the CH$_3$CN $k = 0$ and $k = 1$ components.
[b] No reasonable fits because of multiple velocity components.

are close to recently reported values for low-mass starless cores, indicating that the initial CH$_3$OH abundances at the onset of star formation processes do not vary significantly from low- to high-mass cores.

REFERENCES

Bacmann, A., André, P., Puget, J.-L., et al. 2000, A&A, 361, 555
Beltrán, M. T., Brand, J., Cesaroni, R., et al. 2006, A&A, 447, 221
Beuther, H., Churchwell, E. B., McKee, C. F., & Tan, J. C. 2007, in Protostars and Planets V, ed. B. Reipurth, D. Jewitt, & K. Keil (Tucson: Univ. Arizona Press), 165
Beuther, H., Schilke, P., & Stanke, T. 2003, A&A, 408, 601
Beuther, H., Sridharan, T. K., & Saito, M. 2005a, ApJ, 634, L185
Beuther, H., & Steinacker, J. 2007, ApJ, 656, L85
Beuther, H., et al. 2002, ApJ, 566, 945
———. 2005b, ApJ, 633, 535
Brand, J., & Blitz, L. 1993, A&A, 275, 67
Carey, S. J., Feldman, P. A., Redman, R. O., et al. 2000, ApJ, 543, L157
Churchwell, E. 2002, ARA&A, 40, 27
Codella, C., Bachiller, R., & Reipurth, B. 1999, A&A, 343, 585
Davis, C. J., Varricatt, W. P., Todd, S. P., & Ramsay Howat, S. K. 2004, A&A, 425, 981
Egan, M. P., Shipman, R. F., Price, S. D., et al. 1998, ApJ, 494, L199
Gibb, A. G., Wyrowski, F., & Mundy, L. G. 2004, ApJ, 616, 301
Hildebrand, R. H. 1983, QJRAS, 24, 267
Hill, T., Burton, M. G., Minier, V., et al. 2005, MNRAS, 363, 405
Klein, R., Posselt, B., Schreyer, K., Forbrich, J., & Henning, T. 2005, ApJS, 161, 361
Krumholz, M. R., Klein, R. I., & McKee, C. F. 2007, ApJ, 656, 959
Kurtz, S., Cesaroni, R., Churchwell, E., Hofner, P., & Walmsley, C. M. 2000, Protostars and Planets IV, ed. V. Mannings, A. P. Boss, S. S. Russel (Tuscon: Univ. of Arizona Press), 299
Larson, R. B. 1981, MNRAS, 194, 809
Lefloch, B., Castets, A., Cernicharo, J., & Loinard, L. 1998, ApJ, 504, L109
Loren, R. B., & Mundy, L. G. 1984, ApJ, 286, 232
McKee, C. F., & Tan, J. C. 2002, Nature, 416, 59
———. 2003, ApJ, 585, 850
Molinari, S., Brand, J., Cesaroni, R., & Palla, F. 1996, A&A, 308, 573

Myers, P. C., & Benson, P. J. 1983, ApJ, 266, 309
Myers, P. C., Mardones, D., Tafalla, M., Williams, J. P., & Wilner, D. J. 1996, ApJ, 465, L133
Nomura, H., & Millar, T. J. 2004, A&A, 414, 409
Pei, C. C., & Zeng, Q. 1995a, Acta Astron. Sinica, 36, 20
———. 1995b, Acta Astron. Sinica, 36, 215
Pillai, T., Wyrowski, F., Carey, S. J., & Menten, K. M. 2006, A&A, 450, 569
Poynter, R. L., & Pickett, H. M. 1985, Appl. Opt., 24, 2235
Rathborne, J. M., Jackson, J. M., & Simon, R. 2006, ApJ, 641, 389
Rathborne, J. M., et al. 2005, ApJ, 630, L181
Richer, J. S., Shepherd, D. S., Cabrit, S., Bachiller, R., & Churchwell, E. 2000, Protostars and Planets IV, ed. V. Mannings, A. P. Boss, & S. S. Russell (Tucson: Univ. Arizona Press), 867
Rohlfs, K., & Wilson, T. L. 2006, Tools of Radio Astronomy (4th ed.; Berlin: Springer)
Sanders, D. B., Clemens, D. P., Scoville, N. Z., & Solomon, P. M. 1986, ApJS, 60, 1
Schaller, G., Schaerer, D., Meynet, G., & Maeder, A. 1992, A&AS, 96, 269
Schilke, P., Walmsley, C. M., Pineau des Forets, G., & Flower, D. R. 1997, A&A, 321, 293
Schöier, F. L., van der Tak, F. F. S., van Dishoeck, E. F., & Black, J. H. 2005, A&A, 432, 369
Simon, R., Jackson, J. M., Rathborne, J. M., & Chambers, E. T. 2006, ApJ, 639, 227
Sridharan, T. K., Beuther, H., Saito, M., Wyrowski, F., & Schilke, P. 2005, ApJ, 634, L57
Sridharan, T. K., Beuther, H., Schilke, P., Menten, K. M., & Wyrowski, F. 2002, ApJ, 566, 931
Tafalla, M., Santiago-García, J., Myers, P. C., et al. 2006, A&A, 455, 577
van Dishoeck, E. F., & Blake, G. A. 1998, ARA&A, 36, 317
Zhou, S., Wu, Y., Evans, II, N. J., Fuller, G. A., & Myers, P. C. 1989, ApJ, 346, 168